MATERIALS SCIENCE

Nearly room temperature ferromagnetism in a magnetic metal-rich van der Waals metal

Junho Seo[1,2]*, Duck Young Kim[3]*, Eun Su An[1,2]*, Kyoo Kim[4], Gi-Yeop Kim[5], Soo-Yoon Hwang[5], Dong Wook Kim[6], Bo Gyu Jang[6], Heejung Kim[4], Gyeongsik Eom[7], Seung Young Seo[1,5], Roland Stania[1], Matthias Muntwiler[8], Jinwon Lee[1,2], Kenji Watanabe[9], Takashi Taniguchi[9], Youn Jung Jo[10], Jieun Lee[7], Byung Il Min[2], Moon Ho Jo[1,5], Han Woong Yeom[1,2], Si-Young Choi[5†], Ji Hoon Shim[6†], Jun Sung Kim[1,2†]

In spintronics, two-dimensional van der Waals crystals constitute a most promising material class for long-distance spin transport or effective spin manipulation at room temperature. To realize all-vdW-material–based spintronic devices, however, vdW materials with itinerant ferromagnetism at room temperature are needed for spin current generation and thereby serve as an effective spin source. We report theoretical design and experimental realization of a iron-based vdW material, Fe_4GeTe_2, showing a nearly room temperature ferromagnetic order, together with a large magnetization and high conductivity. These properties are well retained even in cleaved crystals down to seven layers, with notable improvement in perpendicular magnetic anisotropy. Our findings highlight Fe_4GeTe_2 and its nanometer-thick crystals as a promising candidate for spin source operation at nearly room temperature and hold promise to further increase T_c in vdW ferromagnets by theory-guided material discovery.

INTRODUCTION

The isolation of various two-dimensional (2D) van der Waals (vdW) crystals has triggered intensive research on exploring new phenomena in the 2D limit and designing novel devices with tailored functionalities in their heterostructures. Particularly in spintronics, 2D vdW crystals often surpass many known 3D materials because of their exceptional transport-, optical-, and spin-related properties. For example, graphene, the first 2D vdW crystal, turns out to be the best-performing spin channel material with the longest spin diffusion length at room temperature due to its high mobility and low spin-orbit coupling (*1*–*4*). For spin manipulation, spin-valley locking in transition metal dichalcogenides (TMDCs) (*5*, *6*) or spin-momentum locking in the surface state of bismuth chalcogenide–based topological insulators (*7*–*10*) provides unprecedented electrical/optical spin control by their strong spin-orbit coupling (*5*, *6*, *11*–*13*). One missing component is a metallic vdW ferromagnet for spin source, which can generate highly spin-polarized current at room temperature. Despite recent developments on magnetic vdW materials (*14*–*25*), most of the bulk vdW ferromagnets such as $Cr(Si,Ge)Te_3$ (*17*, *18*), $Cr(Br,I)_3$ (*19*, *20*), and Fe_3GeTe_2 (*22*, *23*) have relatively low critical temperatures (T_c), well below the room temperature, which poses a challenge for using magnetic vdW materials in spintronic applications. Recently, the nearly room temperature ferromagnetism was induced in a few-layers-thick Fe_3GeTe_2 crystal by the sophisticated electrolyte gating (*21*). This may not be suitable for realistic spintronic applications but suggests that with proper material design, the room temperature ferromagnetism can be stabilized in a bulk vdW ferromagnet. Very recently, a vdW ferromagnet, $Fe_{5-x}GeTe_2$, has been synthesized, showing $T_c \sim 300$ K, while its crystal structure and the underlying mechanism of high-T_c ferromagnetism have remained as an open question (*26*, *27*). If a stable vdW ferromagnet exists and also has a high conductivity and a large magnetization at room temperature, it can be used as a key component in all-vdW-material–based spintronic applications.

The relatively low T_c of vdW ferromagnets is a consequence of their 2D nature (see Fig. 1, A and B). In the typical TMDC-like structure, each layer of transition metal atoms is encapsulated by chalcogen or halogen atoms (Fig. 1A) and forms a 2D magnetic system with a weak magnetic interlayer coupling across the vdW gap. The pair-exchange interaction is mostly between the neighboring magnetic atoms in the 2D plane and is much weaker than in the 3D magnets. Furthermore, in the 2D limit, the Mermin-Wagner theorem (*28*) states that any continuous symmetry breaking similar to ferromagnetism cannot be spontaneous at a finite temperature. The ferromagnetic (FM) order is therefore stabilized against thermal fluctuations by the uniaxial magnetic anisotropy, and its energy scale K, together with spin-exchange interaction J, determines T_c as $T_c \sim J/\ln(3\pi J/4K)$ in the 2D limit (*29*). Usually, the magnetic anisotropy is set by the magnetocrystalline anisotropy, due to the spin-orbit coupling, and thus is much smaller in energy than exchange interaction, suppressing T_c in vdW ferromagnets. This strongly contrasts to the cases of 3D ferromagnets, in which the spin-exchange interaction J alone determines T_c, as found in, e.g., a bulk iron with $T_c \sim 1000$ K (*30*), much higher than found in vdW ferromagnets.

Our approach to achieve high T_c in vdW ferromagnets is to design a material having a 3D-like network of magnetic elements with enhanced exchange interaction while keeping the vdW structure. This design can be possible if several layers of closely linked magnetic atoms, experiencing 3D-like spin-pair interactions, form the

[1]Center for Artificial Low Dimensional Electronic Systems, Institute for Basic Science (IBS), Pohang 37673, Korea. [2]Department of Physics, Pohang University of Science and Technology, Pohang 37673, Korea. [3]Center for High Pressure Science and Technology Advanced Research, Shanghai, China. [4]Max Planck POSTECH/Hsinchu Center for Complex Phase Materials, Pohang University of Science and Technology, Pohang, Korea. [5]Department of Materials Science and Engineering, Pohang University of Science and Technology, Pohang 37673, Korea. [6]Department of Chemistry, Pohang University of Science and Technology, Pohang 37673, Korea. [7]Department of Physics, Ajou University, Suwon 16499, Korea. [8]Paul Scherrer Institut, 5232 Villigen, Switzerland. [9]National Institute for Materials Science, 1-1 Namiki, Tsukuba 305-0044, Japan. [10]Department of Physics, Kyungpook National University, Daegu 41566, Korea.
*These authors contributed equally to this work.
†Corresponding author. Email: js.kim@postech.ac.kr (J.S.K.); jhshim@postech.ac.kr (J.H.S.); youngchoi@postech.ac.kr (S.-Y.C.)

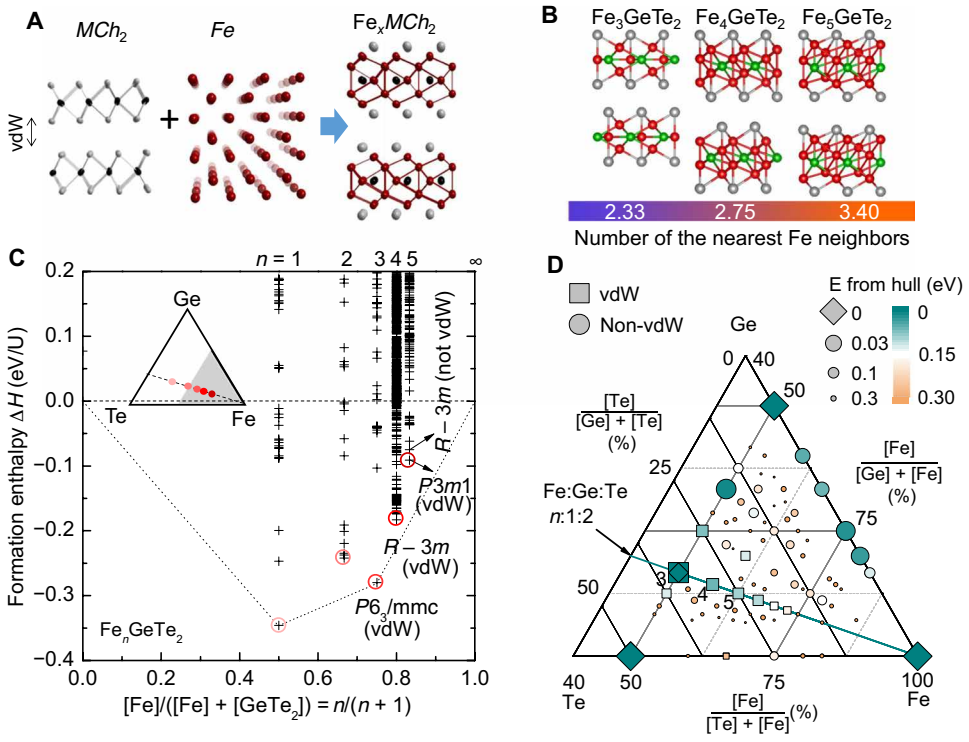

Fig. 1. Material design of Fe-rich van der Waals ferromagnets. (**A**) Schematic illustration of combining two structural motifs of transition metal dichalcogenides MCh_2 (*M*, transition metal; *Ch*, chalcogen) and body-centered cubic iron for Fe-rich vdW ferromagnets Fe_xMCh_2. (**B**) Three stable vdW structures in the series of Fe_nGeTe_2 identified for $n = 3$, 4, and 5 by ab initio calculations. The common structural units of Fe-Fe dumbbells form multiple-layer Fe-rich slabs, which are stacked by vdW coupling. The number of nearest Fe neighbors per Fe atom gradually increases with Fe content *n*, which is expected to be essential to enhance the pair exchange interaction and, thus, T_c. (**C**) Convex hull plot for Fe_nGeTe_2 ($1 \le n \le 5$) with the horizontal decomposition line into Fe and $GeTe_2$. In addition to the thermodynamically stable vdW structure of Fe_3GeTe_2, two additional vdW structures of Fe_nGeTe_2 ($n = 4$, 5) have the low-enough total energy, albeit not on the convex hull line, indicating their possible dynamical stability. (**D**) Ternary phase diagram for various iron-rich compositions, together with the stoichiometry line of Fe:Ge:Te = *n*:1:2. The symbol size and color indicate the proximity to the convex hull plane, and the shape of symbols represents the structure types, including the known stable phases (diamond), vdW type (square), and others (circle). This ternary phase diagram clearly shows relatively stronger stability of the vdW-type Fe_nGeTe_2 phases ($n = 3$, 4, and 5) than their neighbors.

several-atom-thick building blocks, which are stacked by vdW interaction. In such a case, T_c is expected to be increased by enhancing *J* with larger spin-pair interaction and also by suppressing the *K* dependence of T_c. To realize this material design scheme, we propose Fe_nGeTe_2 ($n \ge 3$) as a model system, including two existing metallic ferromagnets, Fe_3GeTe_2 ($T_c = 220$ K) (*22*, *23*) and Fe ($T_c = 1043$ K) (*30*), as the extreme cases. In this material class, magnetically active *n* Fe atoms are linked and stacked with one Ge atom in the unit cell to form a multiple-layered metal-rich slab. This slab is then sandwiched by two Te layers, one above and one below, and becomes suitable for the vdW stacking. Using ab initio calculations, we identified the stable Fe_nGeTe_2 compounds, consisting of Fe-rich thick slabs stacked by vdW coupling. We successfully synthesize a newly designed vdW material Fe_4GeTe_2 that exhibits room temperature ferromagnetism with T_c = 270 K and has a large conductivity, a large magnetic moment, and a low magnetic anisotropy. Fe_4GeTe_2 is therefore a promising spin-source candidate for 2D spintronics based on vdW materials.

RESULTS

Searching for stable crystal structures of Fes_nGeTe_2 ($0 \le n \le 5$) was carried out using the ab initio random structure searching (AIRSS) (*31*) method based on density functional theory (DFT) calculations to predict possible Fe-rich compounds over the existing Fe_3GeTe_2 (*22*, *23*). For the stoichiometry of Fe:Ge:Te = *n*:1:2, we first compare the formation enthalpy (ΔH) of various possible crystal structures and identify the structure with the lowest ΔH.

For $n = 3$, we obtained Fe_3GeTe_2 in the hexagonal vdW structure ($P6_3/mmc$), in excellent agreement with the experimental structure, which confirms the validity of our structural searching approach. The results obtained using the same procedure for $n = 4,5$ are summarized in a convex hull plot, referenced by the decomposition line into Fe and $GeTe_2$ (Fig. 1C). We found that the lowest energy structure in Fe_4GeTe_2 and Fe_5GeTe_2 are close to the convex hull line by ~36 and ~86 meV/atom, respectively. The extended structure prediction on various Fe:Ge:Te compositions in the ternary convex hull surface (Fig. 1D) provides a more general aspect of the energy landscape, revealing that these vdW-type Fe_nGeTe_2 ($n = 4,5$) phases are more stable than the neighboring ones. The proximity to the convex hull surface of each predicted compound, displayed by the symbol size and color, shows a valley-like feature along the stoichiometry line of Fe:Ge:Te = *n*:1:2 ($n \le 3$) in the ternary phase diagram. This suggests that the predicted vdW-type Fe_nGeTe_2 ($n \ge 4$) can be dynamically stabilized while Fe_3GeTe_2 being an energetically stable one. The formation energy of the vdW-type Fe_nGeTe_2 gradually increases with

increasing iron concentration and eventually becomes too close to those of the neighboring compounds above $n = 6$, setting up the theoretical limit of the vdW-type Fe_nGeTe_2.

Our predicted Fe_4GeTe_2 has a rhombohedral structure (space group $R\bar{3}m$) with vdW gap between the layers as shown in Fig. 1B. Similar to Fe_3GeTe_2, Fe_4GeTe_2 has similar structural units of Fe-Fe dumbbells, which are alternatingly off from the plane of Ge atoms and bonded with Te atoms directly. The calculated phonon dispersion of Fe_4GeTe_2 confirms the dynamic stability without any imaginary phonon modes (fig. S1). For Fe_5GeTe_2, the most stable structure also exhibits a vdW structure (space group $P3m1$), which is similar to Fe_4GeTe_2 except that one additional Fe atom is inserted right above the Ge atom (fig. S1D). Its phonon dispersion is also confirmed to be stable (fig. S1). This case, however, includes another non–vdW-type structure (space group $R\bar{3}m$) with a similar formation energy and dynamic stability, in which additional Fe atoms are inserted within the vdW gap of Fe_4GeTe_2 (fig. S1D). Therefore, we expect that in terms of the phase stability, the vdW structure competes with the other structures, including the intercalated one, as the Fe content n increases in the Fe_4GeTe_2 series. Nevertheless, our calculations clearly show that various types of multiple Fe stacking within a $GeTe_2$ layer are possible in the vdW structure, at least for $3 \leq n \leq 5$ (Fig. 1B).

Guided by the material design, we successfully synthesized Fe_4GeTe_2 as a new member in the series of Fe_nGeTe_2 (see Fig. 2). From the systematic synthesis of Fe_xGeTe_2 in a wide range of the Fe content x ($1.5 \leq x \leq 7$), we identified Fe_4GeTe_2 being stable in the vdW structure (fig. S3). High-angle annular dark field (HAADF) scanning transmission electron microscopy (STEM) clearly visualized the vdW gap between the layers and the atomic structure of Fe_4GeTe_2 (Fig. 2, C to E). The thickness of a single layer reaches $d \sim 10$ Å, which is consistent with the results of X-ray diffraction (fig. S3) and of electron beam diffraction (fig. S4). This is much thicker than observed in other magnetic vdW materials, typically $d = 7$ to 8 Å in CrI_3 (*20*) or Fe_3GeTe_2 (*22*, *23*). This difference occurs because Fe and Ge atoms in Fe_4GeTe_2 form a five-atom-thick network, sandwiched by two Te layers, as explained in the plane views of each sublayer of a Fe_4GeTe_2 single layer (Fig. 2A). The weak interlayer vdW coupling in Fe_4GeTe_2 is further confirmed by the fact that it can be easily cleaved using the mechanical exfoliation method and has an atomically flat surface, as seen by scanning tunneling microscopy and atomic force microscopy (figs. S5 and S6).

Between the Te layers, distinctly contrasted in the cross-sectional images (Fig. 2, C and D), the interior Fe atoms are neighbored closest along the c axis in the identical Fe layers (Fe1 or Fe2) and form Fe-Fe dumbbells with a spacing of 2.47 Å. The neighboring Fe atoms between the Fe1 and Fe2 sublayers are also linked with a similar spacing of 2.52 Å. Besides the Fe network, the slightly stronger contrast appears at the Ge sites in the cross-sectional views along $[1\bar{1}0]$ (Fig. 2C) and along [120] (Fig. 2D), consistent with the larger Z-contrast effect of Ge ($Z_{Ge} = 32$) atoms than of Fe (Z_{Fe}=26) atoms. These multilayer building blocks are stacked in the so called ABC configuration in a hexagonal structure (Fig. 2B), yielding a triangular pattern with almost the same contrast in the cross-sectional view along the [001] direction (Fig. 2E). The atomic structure from ab initio calculations (Fig. 2, C to E, inset) and, accordingly, its simulated HAADF STEM images perfectly match with the projection images along the [001], [120], and, particularly, $[1\bar{1}0]$ directions (Fig. 2, C to E). We, thus, conclude that the crystal structure of Fe_4GeTe_2 is rhombohedral (space group $R\bar{3}m$) with lattice parameters $a = 9.97(2)$ Å and $\alpha = 23.3(2)°$, consistent with the x-ray diffraction and x-ray photoelectron diffraction results (figs. S3 and S5), confirming that Fe_4GeTe_2 has the predicted vdW structure. We note that the recently discovered $Fe_{5-x}GeTe_2$, although its precise crystal structure is yet to be identified (*26*, *27*), contains the similar structural motif predicted in our calculations on Fe_4GeTe_2, as discussed in fig. S4.

Now, we focus on the magnetic and transport properties of Fe_4GeTe_2 (Fig. 3). The high-T_c ferromagnetic ordering in Fe_4GeTe_2 was observed by measurements of magnetization $M(T)$ and in-plane resistivity $\rho(T)$ as a function of temperature (Fig. 3A). A clear upturn in the $\chi(T)$ curves for $H||c$ and $H||ab$ indicates an FM transition

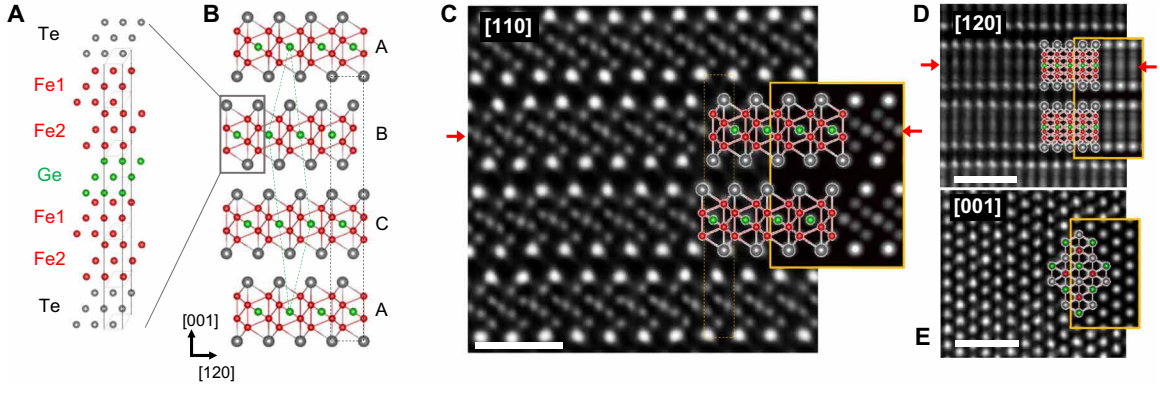

Fig. 2. Crystal structure of Fe_4GeTe_2. (**A**) Stacked plane views of each sublayer along [001] show the seven atomic-thick Fe_4GeTe_2 monolayer. (**B**) Fe_4GeTe_2 monolayers in (A) are stacked in the so-called ABC configuration, resulting in the rhombohedral structure ($R\bar{3}m$) (green dashed lines). The corresponding hexagonal representation (black dashed lines) is also shown for comparison. (**C** to **E**) Scanning transmission electron microscopy (STEM) images along the $[1\bar{1}0]$ (C), [120] (D), and [001] (E) directions with a scale bar of 1 nm. For simplicity, the projection direction is defined using a three-index system in a hexagonal structure. Clear vdW gap between the Fe_4GeTe_2 monolayers is shown in the cross-sectional images along the $[1\bar{1}0]$ (C) and [120] (D) directions. The slightly stronger contrast of the Ge atoms as compared to that of the Fe atoms, which results from the Z-contrast effect, is indicated by the red arrows in (C) and (D). The triangular lattice of atoms with similar contrast in the [001] image (E) is consistent with the ABC stacking. The insets in (C) to (E) show the atomic structures from ab initio calculations and the simulated HAADF STEM images for different projection directions, perfectly matching the measured STEM images.

at $T_c \approx 270$ K, followed by another transition at $T_{SR} = 110$ K, related to the spin reorientation as discussed below. Anomalies in $\rho(T)$ were consistently observed at T_c and T_{SR} but were more clearly visible in its temperature derivative curve $d\rho(T)/dT$ (Fig. 3A). We also obtained $T_c \approx 270$ K from the Arrott's plot of the anomalous Hall effect (AHE) shown in fig. S8. The conductivity σ at T_c of Fe_4GeTe_2 is $\sim 5 \times 10^5$ ohm^{-1}m^{-1}, much larger than those of insulating vdW ferromagnets with $\sigma \sim 10^{-2} - 10^{-3}$ohm^{-1}m^{-1} (*20*, *24*), but comparable with that of Fe_3GeTe_2 (*23*, *25*). The saturation magnetization is $M_{sat} = 1.8\ \mu_B$/Fe atom, which corresponds to a volume magnetization of ~500 electromagnetic unit (emu)/cm^3, larger than M_{sat} = 200 to 340 emu/cm^3 of other vdW ferromagnets (*17*, *20*, *23*, *32*). The high T_c close to room temperature, high conductivity, and large magnetic moment of Fe_4GeTe_2 are obviously strong merits for spin-source materials.

Itinerant ferromagnetism is clearly revealed by the AHE. As found in typical FM metals, the field-dependent magnetization $M(H)$ (Fig. 3C) matches well with the field-dependent transverse conductivity σ_{xy} (Fig. 3D), given as $\sigma_{xy} = \rho_{xy}/\left(\rho_{xx}^2 + \rho_{xy}^2\right)$, where ρ_{xx} and ρ_{xy} are the longitudinal and transverse resistivities, respectively. This indicates that the observed AHE is dominantly determined by the anomalous term $\sigma_{xy}^A = S_H M$, where S_H is the anomalous Hall coefficient, quantifying the strength of the AHE. At high temperatures, $S_H \sim 0.02$ is nearly independent of temperature above T_{SR} but drops significantly below T_{SR}. Accordingly, the anomalous Hall angle $\Theta_{AH} = \sigma_{xy}^A/\sigma_{xx}$ shows a maximum near T_{SR} and decreases to ~0.004 at low temperatures (Fig. 3E). The sensitive response of the AHE to the magnetic transitions at T_c and T_{SR} unambiguously confirms the itinerant nature of the observed ferromagnetism, consistent with electronic structure calculations (fig. S2).

The contrasting properties of Fe_4GeTe_2 to other vdW ferromagnets are manifested by the low-temperature transition at T_{SR}. Comparison of the field-dependent magnetization curves $M(H)$ under $H||c$ and $H||ab$ (Fig. 3C) shows that the magnetic easy axis lies in the *ab*-plane at high temperatures ($T_{SR} < T < T_c$) but is rotated to the *c* axis at temperatures below T_{SR}. Such a spin reorientation transition, without modifying the magnitude of magnetization, is the consequence of the small effective uniaxial magnetic anisotropy (K_{eff}), which originates from two competing contributions, the magnetocrystalline anisotropy (K_m), favoring the easy-axis anisotropy, and the shape anisotropy (K_{sh}), favoring the easy-plane anisotropy. They usually follow different temperature dependences, roughly $K_m \sim M_s^3$ and $K_{sh} \sim M_s^2$, which leads to the temperature-driven spin reorientation transition (Fig. 3B). From the saturation field H_{sat} along the hard axis at low temperatures and the relation of $H_{sat} = 2K_{eff}/M_{sat}$, we estimate that K_{eff} of Fe_4GeTe_2 is ~0.23 J/cm^3, mainly determined by the magnetocrystalline anisotropy of $K_m \sim 0.39$ J/cm^3 with a smaller shape anisotropy of $K_{sh} \sim -0.16$ J/cm^3. This is an order of magnitude smaller than that of Fe_3GeTe_2, showing a strong uniaxial magnetic anisotropy of $K_{eff} = 1.03$ J/cm^3. The small magnetic anisotropy, together with the high T_c, in Fe_4GeTe_2 is clearly off from the trend of other vdW ferromagnets, in which T_c has a positive correlation with the uniaxial

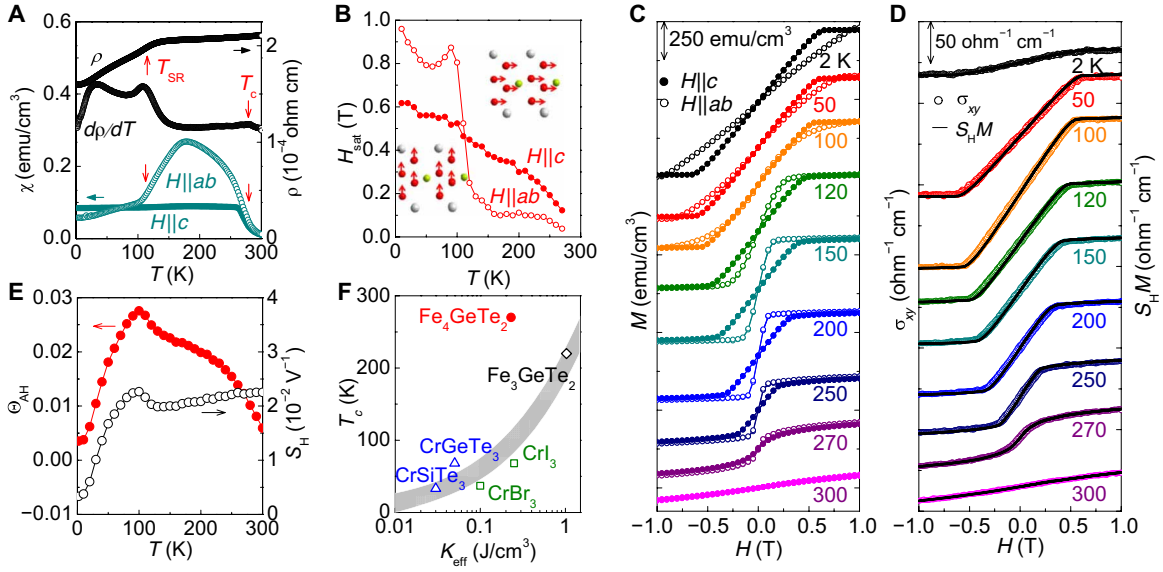

Fig. 3. Magnetotransport properties of Fe_4GeTe_2 single crystal. (**A**) Temperature dependence of the magnetic susceptibility χ (green) at $H = 1$ kOe for different field directions, $H||c$ and $H||ab$, and the electrical resistivity ρ (black, solid symbol) with its temperature derivative $d\rho/dT$ (black, open symbol) with the in-plane current. Both χ(T) and $d\rho/dT(T)$ show anomalies at $T_c = 270$ K, corresponding to the ferromagnetic transition, and at $T_{SR} = 110$ K for the spin-reorientation transition, indicated by red arrows. (**B**) Temperature dependence of the magnetic saturation field H_{sat} for $H||ab$ (open symbols) and $H||c$ (solid symbols). The spin orientation changes from the easy axis ($||c$) to the easy plane (lelab) around $T_{SR} = 110$ K. (**C**) Magnetic field–dependent magnetization $M(H)$ at various temperatures for $H||ab$ (open symbols) and $H||c$ (solid symbols). At temperatures below $T_{SR} = 110$ K, the saturation of $M(H)$ occurs at lower magnetic field for $H||c$ than for $H||ab$, but this relation reverses at higher temperatures below $T_c = 270$ K. (**D**) Magnetic field–dependent Hall conductivity $\sigma_{xy}(H)$ (open symbols) at various temperatures for $H||c$. The magnetic field–dependent magnetization $M(H)$ (solid lines), scaled using the anomalous Hall factor $S_H = \sigma_{xy}^A(H)/M(H)$, matches well with the curves of $\sigma_{xy}(H)$. (**E**) Temperature dependence of the anomalous Hall angle $\Theta_{AH} = \sigma_{xy}^A/\sigma_{xx}$ and the anomalous Hall factor $S_H = \sigma_{xy}^A/M$, showing anomalies at T_{SR}. (**F**) Uniaxial magnetic anisotropy energy K_{eff} and the FM transition temperature T_c for various vdW ferromagnets, CrX_3 (X = Br, I) (*19*, *20*), $CrMTe_2$ (M = Si, Ge) (*17*, *32*), and Fe_4GeTe_2 (*23*, *25*) (n = 3, 4). The positive correlation between T_c and K in vdW ferromagnets is indicated by the shaded line.

magnetic anisotropy energy K_{eff} (Fig. 3F). This suggests that the enhanced J is responsible for the high T_c in Fe_4GeTe_2, where a large spin-pair interaction is expected in the network of Fe atoms.

The observed high-T_c ferromagnetism and high conductivity are well retained in nanometer-thick Fe_4GeTe_2 flakes, as confirmed by magnetic circular dichroism (MCD) and AHE measurements (Fig. 4). The MCD signal, obtained in the seven-layer-thick (7L) flake with a small external field H = 0.5 T, clearly exhibits the FM transition at $T_c \sim 270$ K. With a zero external field, however, the MCD is nearly zero above $T_{SR} \sim 200$ K but becomes finite below T_{SR} with a magnetic domain structure with a typical size of a few micrometers. Since MCD probes the out-of-plane component of magnetization, this confirms the spin-reorientation transition. The high T_c and the high conductivity for nanoflakes are confirmed by the magnetotransport measurements, $\rho(T)$ (Fig. 4D) and $\sigma^A_{xy}(H)$ (Fig. 4E). The spontaneous component of $\sigma^A_{xy,S}(T)$, estimated from the Arrot plot of $\sigma^A_{xy}(H)$ at different temperatures for nanoflakes with various thicknesses (fig. S8), shows a clear onset at $T_c \sim 270$ K (Fig. 4F), indicating that T_c remains almost the same or slightly increased with lowering the thickness (Fig. 4G).

Unlike high T_c and conductivity, the magnetic anisotropy and the magnetic coercivity are more significantly controlled by reducing the thickness. As shown in Fig. 4E and fig. S9, magnetic hysteresis curves of $\sigma^A_{xy}(H)$ become square shaped with a large coercive field $H_c \sim 1000$ Oe. The remnant magnetization (M_R) with respect to M_{sat}, estimated from $\sigma^A_{xy}(H = 0)/\sigma^A_{xy}(H_{sat})$, approaches to ~1 in nanoflakes at low temperatures, but it is suppressed above T_{SR} (fig. S9). The spin-reorientation temperature T_{SR} is significantly enhanced up to ~200 K with lowering the thickness down to 7L, extending the temperature range of perpendicular magnetic anisotropy (PMA). Consistently, the saturation field H_{sat} along the in plane, i.e., the magnetic hard axis, estimated from the angle-dependent AHE experiments (fig. S10) is almost six times larger than the bulk value. This implies that the surface magnetic anisotropy becomes dominant in nanoflakes, inducing strong enhancement of PMA, which is known to be critical to thermal stability and magnetic remanence. Although the observed increase in PMA is not sufficient to maintain magnetic remanence close to T_c, our findings strongly suggest that the magnetic anisotropy of Fe_4GeTe_2 nanoflakes can be further controlled with proper surface modification while keeping high-T_c ferromagnetism.

DISCUSSION

One of the most critical questions is the origin of the observed increase in T_c in Fe_4GeTe_2 with respect to Fe_3GeTe_2. To theoretically understand this question, we used DFT calculations, combined with dynamic mean field theory (DMFT) on the series of Fe_nGeTe_2 ($3 \leq n \leq 5$). Since the calculations based on the mean field theory are known to overestimate T_c and the saturation magnetization M_{sat}, we scaled them against those of Fe_3GeTe_2 (T_c = 220 K) and compared their relative changes, as shown in Fig. 5A. The resulting saturation magnetic moment as a function of temperature shows that T_c and M_{sat} increase in Fe_4GeTe_2 by ~21 and ~ 16%, respectively. These

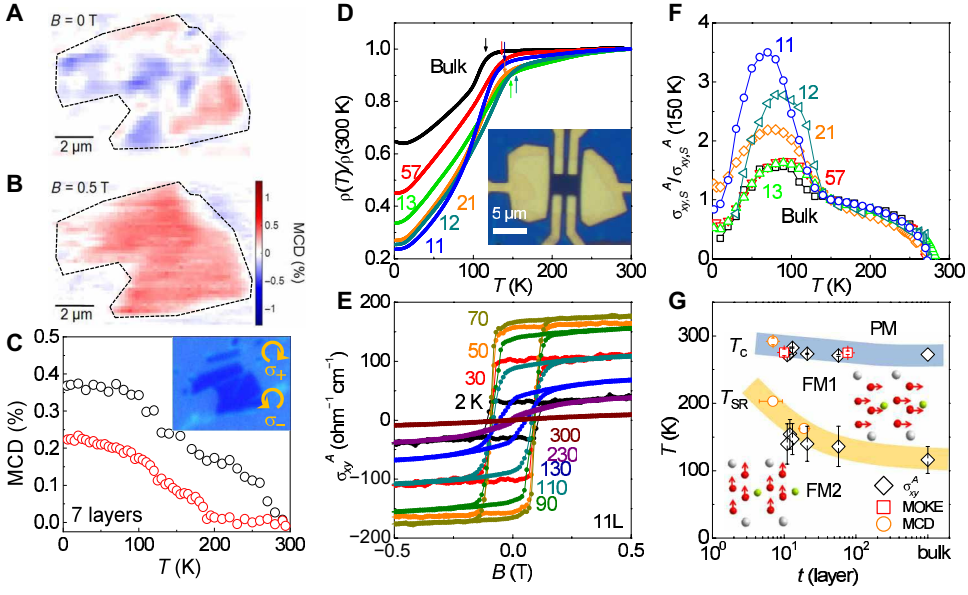

Fig. 4. Thickness-dependent magnetic properties and phase diagram of Fe_4GeTe_2 nanoflakes. (**A** and **B**) Magnetic circular dichroism (MCD) image of a seven-layer-thick (7L) Fe_4GeTe_2 crystal at B = 0 T (A) and B = 0.5 T (B). (**C**) The corresponding temperature-dependent MCD signal with B = 0 T (red) and B = 0.5 T (black), showing both ferromagnetic and spin-reorientation temperatures T_c and T_{SR}. The inset shows the optical image of the 7L Fe_4GeTe_2 crystal and the circular polarizations for MCD measurements. (**D**) Temperature dependence of the normalized in-plane resistivity $\rho(T)$ for cleaved Fe_4GeTe_2 crystals with various thicknesses, indicated by numbers of the layers. The optical image of a typical device of BN-covered Fe_4GeTe_2 crystals. (**E**) Field-dependent Hall conductivity (σ_{xy}) for a 11-layer-thick Fe_4GeTe_2 crystal, revealing AHE with a clear hysteresis. (**F**) Temperature dependence of the spontaneous anomalous Hall conductivity ($\sigma^A_{xy,S}$), normalized by $\sigma^A_{xy,S}$(150 K), indicating its clear onset at T_c for all cleaved crystals. (**G**) Thickness-dependent phase diagram of Fe_4GeTe_2 crystal with T_c and T_{SR}, estimated from resistivity, AHE, MCD, and magneto-optical Kerr effect (MOKE) measurements. Significant enhancement of T_{SR} with lowering thickness contrasts to the nearly constant $T_c \sim 270$ K and is consistent with a strong enhancement of perpendicular magnetic anisotropy.

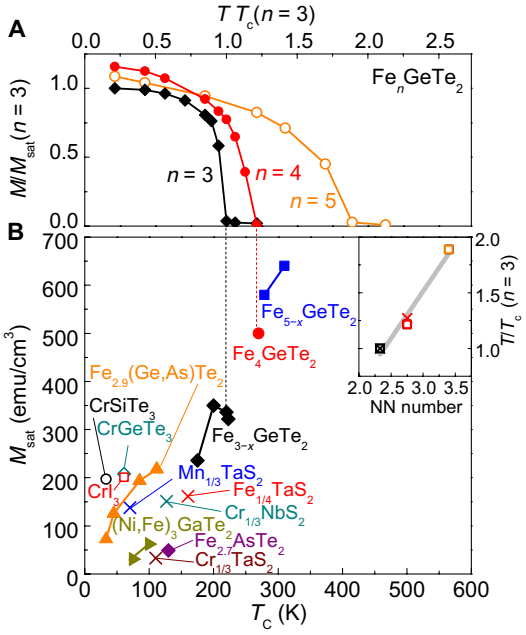

Fig. 5. Magnetic properties of Fe_4GeTe_2 in comparison with other vdW ferromagnets. (**A**) Calculated magnetization for Fe_nGeTe_2 as a function of temperature. The temperature and the magnetization per Fe atom are normalized by those of Fe_3GeTe_2 to show their relative changes. (**B**) Ferromagnetic transition temperature T_c and saturation magnetization M_{sat} for various vdW-type ferromagnets, including Cr-based insulating vdW ferromagnets (open symbols) (*17*, *20*, *32*), Fe-based metallic vdW ferromagnets (solid symbols) (*23*, *25*–*27*, *40*–*42*), and the ferromagnetic TMDC compounds (crosses) with intercalation of magnetic transition metal atoms (M = Fe, Cr, and Mn) (*43*–*46*). Among them, Fe_nGeTe_2 compounds exhibit high T_c and high M_{sat}. The inset shows that calculated (open) and measured (cross) T_c's of Fe_nGeTe_2, normalized by that of Fe_3GeTe_2, increase almost linearly with the number of the nearest Fe neighbors (NN) per Fe atom.

results are in good agreement with experiments for Fe_3GeTe_2, showing the relative increases of ~27% in T_c and ~29% in M_{sat}, compared with Fe_3GeTe_2. The similar increase in T_c with increasing n is also predicted for hypothetical Fe_3GeTe_2 (n = 5), as shown in Fig. 5A. In the recently discovered $Fe_{5-x}GeTe_2$, T_c for bulk samples is enhanced up to ~310 K (*26*, *27*), which is less than our prediction, presumably due to Fe deficiency, but consistently follows the expected trend. This systematic increase in T_c with n is consistent with the enhancement of FM spin-pair interaction, which is usually proportional to the number of the nearest neighbor (NN) Fe—Fe bonds. We found that T_c of Fe_nGeTe_2 depends almost linearly on the number of NN Fe bonds (the inset of Fig. 5B) despite the different electronic structures (fig. S2). This corroborates that the dominant mechanism determining T_c is the FM spin-pair interaction in the network of Fe atoms within the relatively thick layers.

Our findings highlight that Fe-rich vdW ferromagnets are promising spin-source materials. To work well as a spin source, a candidate material should satisfy several conditions, including high T_c for room temperature operation, high M_{sat} for high spin polarization, metallic conductivity for relatively easy spin injection, and PMA for high density integration. In comparison with other vdW ferromagnets or intercalated vdW ferromagnets reported so far, Fe_4GeTe_2 shows high T_c and high M_{sat} (Fig. 5B) and, thus, is a candidate, satisfying the most of requirements, except the PMA condition. The weak PMA property and a small magnetic remanence of bulk Fe_4GeTe_2 can be further tailored by reducing its thickness down to a few layers, leading to strong increase in both PMA and T_{SR}, together with a hard magnet–type hysteresis. These results clearly demonstrate the synergetic combination of material design and thickness control on vdW magnets, which improves the magnetic properties more suitable for realistic spintronic applications. Furthermore, the not-yet-synthesized stoichiometric compound Fe_5GeTe_2 (*26*, *27*, *33*) or Fe_4GeTe_2 nanoflakes with proper surface modification using, e.g., electrolyte gating (*21*), are expected to exhibit better ferromagnetic properties with even higher T_c or stronger magnetic remanence. We therefore envision that the heterostructures of Fe_nGeTe_2 and other vdW materials with surpassing spin-related properties at room temperatures, including graphene as an effective spin channel, TMDCs as optical or electrical control of spin dynamics, or bismuth chalcogenide–based topological insulators for spin-orbit torque operation, will open a new avenue for realizing all-vdW-material-based spintronic devices at room temperature.

MATERIALS AND METHODS

First principles calculations

To explore computationally the energy landscape of Fe_nGeTe_2 compounds, we performed crystal structure searching using AIRSS strategy (AIRSS, version 0.91) (*31*), combined with a plane wave–based DFT software. A plane wave basis set cutoff energy of 300 eV and k-points sampling of 0.06 $Å^{-1}$ were used. AIRSS generated ~11,000 trial structures to find the ground states of various stoichiometric compounds. Phonon dispersions were calculated using density functional perturbation theory (*34*), implemented in the VASP software and phonopy software (*35*). Electronic structure calculations within the DFT were performed by using the full-potential linearized augmented plane wave code WIEN2k (*36*). In the DFT + DMFT code, the DFT part was done by the WIEN2K software with Perdew-Burke-Ernzerhof exchange correlation potential (*37*). The DMFT part dealt with the correlation of d orbitals in Fe atoms. DFT + DMFT loops were operated in a charge self-consistent manner (*38*). For the impurity solver, a continuous time quantum Monte Carlo method was used with interaction parameters of Hubbard U = 5.0 eV and Hund J_H = 1.2 eV (*39*). In these calculations, we used experimental lattice constants for Fe_3GeTe_2 and Fe_4GeTe_2, whereas we used for the hypothetical vdW structure (space group $P3m1$) from the AIRSS results for Fe_5GeTe_2.

Scanning transmission electron microscopy

Three kinds of samples having [120], [001], and [1$\bar{1}$0] projections were prepared using dual-beam focused ion beam systems (Helios and Helios G3, FEI) to determine the 3D crystal structure. Because Fe_4GeTe_2 single crystal was formed in the shape of a thin hexagonal flake, the crystallographic directions can be easily determined. We used a Ga ion beam at 30 kV to make a thin specimen and then used different acceleration voltages from 5 to 1 kV for the sample cleaning process to reduce the Ga damage. The selected area diffraction pattern analysis and atomic structure observation were performed using a STEM (JEM-ARM200F, JEOL, Japan) at 200 kV equipped with an fifth-order probe corrector (ASCOR, CEOS GmbH, Germany). The optimum size of the electron probe for STEM observation was ~78 pm. The collection semiangles of the HAADF detector were adjusted from 68 to 280 mrad to collect scattered electrons in a large angle for clear Z-sensitive images. The annular bright field images

were obtained using a 6-mm aperture and a collection angle from 10 to 20 mrad. The obtained raw images were processed using a bandpass Wiener filter with a local window to reduce background noise (Filters Pro, HREM Research Inc., Japan). TEM diffraction pattern simulation was performed using SingleCrystal (CrystalMaker Software Ltd., UK). STEM image simulation was performed by using the multislice method implemented in the QSTEM software (shareware, http://qstem.org).

Single crystal growth and bulk properties

For single crystal growth, we used a presynthesized polycrystalline sample of Fe_4GeTe_2. A mixture of Fe (99.998%), Ge (99.999%), and Te (99.999%) in the molar ratio of x:1:2 ($1.5 \leq x \leq 7$) was placed in an evacuated quartz tube that was heated at 725°C for 10 days. The stoichiometry ratio of Fe:Ge:Te = 5:1:2 in the starting mixture was found to be optimal to produce single-phase polycrystalline Fe_4GeTe_2 samples (fig. S3A), which were then used for single crystal growth by a chemical vapor transport method using iodine as a transport agent. Polycrystalline Fe_4GeTe_2 was placed in an evacuated quartz tube together with iodine of 1.8 mg/cm^3, which was heated at 800°C/750°C with a temperature gradient of 5°C/cm for 7 days. The obtained single crystals were in a plate shape with a typical size of $\sim 1 \times 1 \times 0.04$ mm^3 as shown in the inset of fig. S3B. The x-ray diffraction confirms high crystallinity (fig. S3B), in good agreement with STEM experiments (Fig. 2). The energy dispersive spectroscopy revealed that the stoichiometry of the single crystal was Fe:Ge:Te = 4.11:1.0:1.85, i.e., a slight Te deficiency of ~15%. The presence of Te deficiency was also confirmed by STM on the cleaved and mostly Te-terminated surface (fig. S5A). Magnetization was measured under a magnetic field along the c axis or ab-plane using a superconducting quantum interference device magnetometer (Magnetic Properties Measurement System, Quantum Design). The in-plane resistivity and Hall coefficient were measured in the standard six-probe configuration using a Physical Property Measurement System (PPMS-14T, Quantum Design).

Mechanical exfoliation and device fabrication

Because of weak vdW coupling between the layers in Fe_4GeTe_2, we were able to obtain the thin flakes of Fe_4GeTe_2 using mechanical exfoliation. We used Si substrates terminated by a 270-nm-thick SiO_2 layer, which was cleaned in acetone, 2-propanol, and deionized water and then treated by oxygen plasma (O_2 = 10 sccm, $P \sim 100$ mtorr) for 5 min to remove adsorbates from the surface. Fe_4GeTe_2 single crystal was cleaved on the tape to make several flakes, which were brought into contact to the Si/SiO_2 substrate. All the cleaving and handling were done in the inert atmosphere with pure Ar [H_2O < 0.1 parts per million (ppm), O_2 < 0.1 ppm] gas, except the atomic force microscopy measurements. The obtained flakes were typically several micrometers squared in area and ~10 nm in thickness (~10 layers). Rarely, we found even a thinner flake with a thickness of ~7 nm (7 layers) but smaller in size. For device fabrication, thin exfoliated crystals of h-BN were subsequently transferred onto the ultrathin Fe_4GeTe_2 crystal in argon atmosphere. Electrodes for the transport measurements were fabricated by the electron beam lithography technique using poly(methyl methacrylate)-positive resist layer, which was spin coated and dried in vacuum. The patterned area on the ultrathin crystal was etched by ion milling, followed by deposition of Cr(10 nm)/Au(50 nm). We note that during device fabrication, ultrathin crystals were always in room temperature without postheating and not exposed to air, which was found to be critical to minimize the chemical degradation of the surface.

Magneto-optical and magnetotransport property measurements for nanoflake devices

For MCD measurements, a continuous-wave laser with wavelength at 664 nm (P = 60 μW) was focused onto the thin flakes of Fe_4GeTe_2. The polarization of the incident laser was altered between the right and left circular polarization at the frequency of 50 kHz using a photoelastic modulator, and lock-in detection was used to measure the absorption difference between two helicities of light. To obtain the 2D mapping of the MCD signal, we scanned the sample position using an xy piezo stage with the beam spot size of ~0.7 μm. For all measurements, we mounted samples in an optical cryostat with or without a magnet in Faraday geometry. For magneto-optical Kerr effect measurements, a continuous-wave laser with 532 nm (P = 100 μW) was linearly polarized at 45° to the photoelastic modulator fast axis. The linearly polarized light transmitted through the photoelastic modulator with phase modulation frequency of 50 kHz and phase retardation of λ/2, and it was focused onto the sample at normal incidence. The reflected light from the sample was analyzed using Wollaston prism for splitting the orthogonal components of light, and the power difference was detected using balanced photodiode and lock-in amplifier. Permanent magnet in Faraday geometry with 0.1 T was adjusted, and the temperature of the sample was controlled in the optical cryostat. The in-plane resistivity and Hall resistivity of the Fe_4GeTe_2 nanoflakes were measured in standard six-probe configuration using a PPMS (PPMS-14T, Quantum Design). The alternating current with amplitude of a few microamperes and the frequency of ~13 Hz was used for lock-in measurements of longitudinal and Hall resistance. For the AHE measurements at various field orientations, a one-axis rotator was used in PPMS-14T with a typical angle resolution of ~1°.

SUPPLEMENTARY MATERIALS

Supplementary material for this article is available at http://advances.sciencemag.org/cgi/content/full/6/3/eaay8912/DC1

Supplementary Text
Note S1. Material design for Fe_nGeTe_2.
Note S2. Material synthesis.
Note S3. TEM on Fe_4GeTe_2.
Note S4. Surface characterization on Fe_4GeTe_2 single crystal.
Note S5. Ultrathin Fe_4GeTe_2 nanoflakes and their magnetic properties.
Fig. S1. Material design for Fe_nGeTe_2.
Fig. S2. Electronic structures of Fe_nGeTe_2.
Fig. S3. Material synthesis of designed Fe_nGeTe_2.
Fig. S4. TEM on Fe_4GeTe_2.
Fig. S5. Surface characterization on Fe_4GeTe_2 single crystal.
Fig. S6. Ultrathin Fe_4GeTe_2 nanoflakes and their magneto-optical properties.
Fig. S7. Thickness dependence of resistivity for Fe_4GeTe_2 nanoflakes.
Fig. S8. Thickness-dependent AHE of Fe_4GeTe_2 nanoflakes.
Fig. S9. Thickness-dependent magnetic hysteresis behaviors of Fe_4GeTe_2 nanoflakes.
Fig. S10. Enhanced PMA of Fe_4GeTe_2 nanoflakes.
References (*47*–*53*)

REFERENCES AND NOTES

1. D. Pesin, A. H. MacDonald, Spintronics and pseudospintronics in graphene and topological insulators. *Nat. Mater.* **11**, 409–416 (2012).
2. W. Han, R. K. Kawakami, M. Gmitra, J. Fabian, Graphene spintronics. *Nat. Nanotechnol.* **9**, 794–807 (2014).
3. M. Drogeler, C. Franzen, F. Volmer, T. Pohlmann, L. Banszerus, M. Wolter, K. Watanabe, T. Taniguchi, C. Stampfer, B. Beschoten, Spin lifetimes exceeding 12 ns in graphene nonlocal spin valve devices. *Nano Lett.* **16**, 3533–3539 (2016).

4. J. Ingla-Aynés, R. J. Meijerink, B. J. van Wees, Eighty-eight percent directional guiding of spin currents with 90 μm relaxation length in bilayer graphene using carrier drift. *Nano Lett.* **16**, 4825–4830 (2016).
5. L. Yang, N. A. Sinitsyn, W. Chen, J. Yuan, J. Zhang, J. Lou, S. A. Crooker, Long-lived nanosecond spin relaxation and spin coherence of electrons in monolayer MoS_2 and WS_2. *Nat. Phys.* **11**, 830–834 (2015).
6. Q. H. Wang, K. Kalantar-Zadeh, A. Kis, J. N. Coleman, M. S. Strano, Electronics and optoelectronics of two-dimensional transition metal dichalcogenides. *Nat. Nanotechnol.* **7**, 699–712 (2012).
7. A. R. Mellnik, J. S. Lee, A. Richardella, J. L. Grab, P. J. Mintun, M. H. Fischer, A. Vaezi, A. Manchon, E. A. Kim, N. Samarth, D. C. Ralph, Spin-transfer torque generated by a topological insulator. *Nature* **511**, 449–451 (2014).
8. K. Kondou, R. Yoshimi, A. Tsukazaki, Y. Fukuma, J. Matsuno, K. S. Takahashi, M. Kawasaki, Y. Tokura, Y. Otani, Fermi-level-dependent charge-to-spin current conversion by Dirac surface state of topological insulators. *Nat. Phys.* **12**, 1027–1031 (2016).
9. Y. Wang, D. Zhu, Y. Wu, Y. Yang, J. Yu, R. Ramaswamy, R. Mishra, S. Shi, M. Elyasi, K.-L. Teo, Y. Wu, H. Yang, Room temperature magnetization switching in topological insulator-ferromagnet heterostructures by spin-orbit torques. *Nat. Commun.* **8**, 1364 (2017).
10. J. Han, A. Richardella, S. A. Siddiqui, J. Finley, N. Samarth, L. Liu, Room-temperature spin-orbit torque switching induced by a topological insulator. *Phys. Rev. Lett.* **119**, 077702 (2017).
11. C. Jin, J. Kim, M. I. B. Utama, E. C. Regan, H. Kleemann, H. Cai, Y. Shen, M. J. Shinner, A. Sengupta, K. Watanabe, T. Taniguchi, S. Tongay, A. Zettl, F. Wang, Imaging of pure spin-valley diffusion current in WS_2-WSe_2 heterostructures. *Science* **360**, 893–896 (2018).
12. A. Dankert, S. P. Dash, Electrical gate control of spin current in van der Waals heterostructures at room temperature. *Nat. Commun.* **8**, 16093 (2017).
13. Z. Wang, D. K. Ki, H. Chen, H. Berger, A. H. MacDonald, A. F. Morpurgo, Strong interface-induced spin-orbit interaction in graphene on WS_2. *Nat. Commun.* **6**, 8339 (2015).
14. K. S. Burch, D. Mandrus, J.-G. Park, Magnetism in two-dimensional van der Waals materials. *Nature* **563**, 47–52 (2018).
15. B. Huang, G. Clark, E. Navarro-Moratalla, D. R. Klein, R. Cheng, K. L. Seyler, D. Zhong, E. Schmidgall, M. A. McGuire, D. H. Cobden, W. Yao, D. Xiao, P. Jarillo-Herrero, X. Xu, Layer-dependent ferromagnetism in a van der Waals crystal down to the monolayer limit. *Nature* **546**, 270–273 (2017).
16. C. Gong, L. Li, Z. Li, H. Ji, A. Stern, Y. Xia, T. Cao, W. Bao, C. Wang, Y. Wang, Z. Q. Qiu, R. J. Cava, S. G. Louie, J. Xia, X. Zhang, Discovery of intrinsic ferromagnetism in two-dimensional van der Waals crystals. *Nature* **546**, 265–269 (2017).
17. L. D. Casto, A. J. Clune, M. O. Yokosuk, J. L. Musfeldt, T. J. Williams, H. L. Zhuang, M.-W. Lin, K. Xiao, R. G. Hennig, B. C. Sales, J.-Q. Yan, D. Mandrus, Strong spin-lattice coupling in $CrSiTe_3$. *APL Mater.* **3**, 041515 (2015).
18. V. Carteaux, D. Brunet, G. Ouvrard, G. Andre, Crystallographic, magnetic and electronic structures of a new layered ferromagnetic compound $Cr_2Ge_2Te_6$. *J. Phys. Condens. Matter* **7**, 69–87 (1995).
19. I. Tsubokawa, On the magnetic properties of a $CrBr_3$ single crystal. *J. Physical Soc. Japan* **15**, 1664–1668 (1960).
20. M. A. McGuire, H. Dixit, V. R. Cooper, B. C. Sales, Coupling of crystal structure and magnetism in the layered, ferromagnetic insulator CrI_3. *Chem. Mater.* **27**, 612–620 (2015).
21. Y. Deng, Y. Yu, Y. Song, J. Zhang, N. Z. Wang, Z. Sun, Y. Yi, Y. Z. Wu, S. Wu, J. Zhu, J. Wang, X. H. Chen, Y. Zhang, Gate-tunable room-temperature ferromagnetism in two-dimensional Fe_3GeTe_2. *Nature* **563**, 94–99 (2018).
22. H.-J. Deiseroth, K. Aleksandrov, C. Reiner, L. Kienle, R. K. Kremer, Fe_3GeTe_2 and Ni_3GeTe_2 - two new layered transition-metal compounds: Crystal structures, HRTEM investigations, and magnetic and electrical properties. *Eur. J. Inorg. Chem.* **2006**, 1561–1567 (2006).
23. B. Chen, J. Yang, H. Wang, M. Imai, H. Ohta, C. Michioka, K. Yoshimura, M. Fang, Magnetic properties of layered itinerant electron ferromagnet Fe_3GeTe_2. *J. Physical Soc. Japan* **82**, 124711 (2013).
24. B. Siberchicot, S. Jobic, V. Carteaux, P. Gressier, G. Ouvrard, Band structure calculations of ferromagnetic chromium tellurides $CrSiTe_3$ and $CrGeTe_3$. *J. Phys. Chem.* **100**, 5863–5867 (1996).
25. K. Kim, J. Seo, E. Lee, K. -T. Ko, B. S. Kim, B. G. Jang, J. M. Ok, J. Lee, Y. J. Jo, W. Kang, J. H. Shim, C. Kim, H. W. Yeom, B. I. Min, B. J. Yang, J. S. Kim, Large anomalous Hall current induced by topological nodal lines in a ferromagnetic van der Waals semimetal. *Nat. Mater.* **17**, 794–799 (2018).
26. J. Stahl, E. Shlaen, D. Johrendt, The van der Waals ferromagnets $Fe_{5-\delta}GeTe_2$ and $Fe_{5-\delta-x}Ni_xGeTe_2$ - Crystal structure, stacking faults, and magnetic properties. *Z. Anorg. Allg. Chem.* **644**, 1923–1929 (2018).
27. A. F. May, D. Ovchinnikov, Q. Zheng, R. Hermann, S. Calder, B. Huang, Z. Fei, Y. Liu, X. Xu, M. A. McGuire, Ferromagnetism near room temperature in the cleavable van der Waals crystal Fe_5GeTe_2. *ACS Nano* **13**, 4436–4442 (2019).
28. N. D. Mermin, H. Wagner, Absence of ferromagnetism or antiferromagnetism in one- or two-dimensional isotropic Heisenberg models. *Phys. Rev. Lett.* **17**, 1133–1136 (1966).
29. M. Bander, D. L. Mills, Ferromagnetism of ultrathin films. *Phys. Rev. B* **38**, 12015–12018 (1988).
30. J. R. Hook, H. E. Hall, *"[Ferromagntism]" in Solid State Physics* (Wiley, Chichester, ed. 2, 1991), pp. 226.
31. C. J. Pickard, R. J. Needs, Ab initio random structure searching. *J. Phys. Condens. Matter* **23**, 053201 (2011).
32. H. Ji, R. A. Stokes, L. D. Alegria, E. C. Blomberg, M. A. Tanatar, A. Reijnders, L. M. Schoop, T. Liang, R. Prozorov, K. S. Burch, N. P. Ong, J. R. Petta, R. J. Cava, A ferromagnetic insulating substrate for the epitaxial growth of topological insulators. *J. Appl. Phys.* **114**, 114907 (2013).
33. F. Spirovski, C. Reiner, H.-J. Deiseroth, L. Kienle, H. Mikus, M_3GeTe_2 and M_5GeTe_2 - new layered tellurides (M = Fe, Ni). *Z. Anorg. Allg. Chem.* **632**, 2103–2103 (2006).
34. S. Baroni, S. de Gironcoli, A. Dal Corso, P. Giannozzi, Phonons and related crystal properties from density-functional perturbation theory. *Rev. Mod. Phys.* **73**, 515–562 (2001).
35. A. Togo, I. Tanaka, First principles phonon calculations in materials science. *Scr. Mater.* **108**, 1–5 (2015).
36. A. P. Blaha, K. Schwarz, G. K. H. Madsen, D. Kvasnicka, J. Luitz, *WIEN2k, an augmented plane wave + local orbitals program for calculating crystal properties* (Karlheinz Schwartz, Techn. Universitat Wien, Austria, 2001).
37. J. P. Perdew, K. Burke, M. Ernzerhof, Generalized gradient approximation made simple. *Phys. Rev. Lett.* **77**, 3865–3868 (1996).
38. K. Haule, C.-H. Yee, K. Kim, Dynamical mean-field theory within the full-potential methods: electronic structure of $CeIrIn_5$, $CeCoIn_5$, and $CeRhIn_5$. *Phys. Rev. B* **81**, 195107 (2010).
39. K. Haule, Quantum Monte Carlo impurity solver for cluster dynamical mean-field theory and electronic structure calculations with adjustable cluster base. *Phys. Rev. B* **75**, 155113 (2007).
40. D. Yuan, S. Jin, N. Liu, S. Shen, Z. Lin, K. Li, X. Chen, Tuning magnetic properties in quasi-two-dimensional ferromagnetic $Fe_{3-y}Ge_{1-x}As_xTe_2$ ($0 \le x \le 0.85$). *Mater. Res. Express* **4**, 036103 (2017).
41. A. N. Kuznetsov, E. A. Stroganova, E. Y. Zakharova, A. V. Solopchenko, A. V. Sobolev, I. A. Presniakov, D. I. Kirdyankin, V. M. Novotortsev, Mixed nickel-gallium tellurides $Ni_{3-x}GaTe_2$ as a matrix for incorporating magnetic cations: A $Ni_{3-x}Fe_xGaTe_2$ series. *J. Solid State Chem.* **250**, 90–99 (2017).
42. V. Y. Verchenko, S. S. Sokolov, A. A. Tsirlin, A. V. Sobolev, I. A. Presniakov, M. A. Bykov, M. A. Kirsanova, A. V. Shevelkov, New Fe-based layered telluride $Fe_{3-\delta}As_{1-y}Te_2$: Synthesis, crystal structure and physical properties. *Dalton Trans.* **45**, 16938–16947 (2016).
43. J. G. Checkelsky, M. Lee, E. Morosan, R. J. Cava, N. P. Ong, Anomalous Hall effect and magnetoresistance in the layered ferromagnet $Fe_{1/4}TaS_2$. *Phys. Rev. B* **77**, 014433 (2008).
44. T. Miyadai, K. Kikuchi, H. Kondo, S. Sakka, M. Arai, Y. Ishikawa, Magnetic properties of $Cr_{1/3}NbS_2$. *J. Phys. Soc. Jpn* **52**, 1394 (1983).
45. H. Zhang, W. Wei, G. Zheng, J. Lu, M. Wu, X. Zhu, J. Tang, W. Ning, Y. Han, L. Ling, J. Yang, W. Gao, Y. Qin, M. Tian, Electrical and anisotropic magnetic properties in layered $Mn_{1/3}TaS_2$ crystals. *Appl. Phys. Lett.* **113**, 072402 (2018).
46. Y. Yamasaki, R. Moriya, M. Arai, S. Masubuchi, S. Pyon, T. Tamegai, K. Ueno, T. Machida, Exfoliation and van der Waals heterostructure assembly of intercalated ferromagnet $Cr_{1/3}TaS_2$. *2D Mater.* **4**, 041007 (2017).
47. H.-J. Deiseroth, F. Spirovski, C. Reiner, M. Schlosser, Crystal structures of nickel germanium selenide, $Ni_{5.45}GeSe_2$, and nickel germanium telluride, $Ni_{5.45}GeTe_2$. *Z. Kristallogr. New Cryst. Struct.* **222**, 171–172 (2007).
48. A. F. May, S. Calder, C. Cantoni, H. Cao, M. A. McGuire, Magnetic structure and phase stability of the van der Waals bonded ferromagnet $Fe_{3-x}GeTe_2$. *Phys. Rev. B* **93**, 014411 (2016).
49. C. S. Fadley, Angle-resolved X-ray photoelectron spectroscopy. *Prog. Surf. Sci.* **16**, 275–388 (1984).
50. J. Osterwalder, T. Greber, A. Stuck, L. Schlapbach, Experimental full-solid-angle substrate photoelectron-diffraction data at 1-keV energies: Implications for photoelectron holography. *Phys. Rev. B* **44**, 13764 (1991).
51. P. Oberta, U. Flechsig, M. Muntwiler, C. Quitmann, Optical design study of the PEARL beamline at SLS. *Nucl. Instrum. Methods Phys. Res. A* **635**, 116–120 (2011).
52. M. Muntwiler, J. Zhang, R. Stania, F. Matsui, P. Oberta, U. Flechsig, L. Patthey, C. Quitmann, T. Glatzel, R. Widmer, E. Meyer, T. A. Jung, P. Aebi, R. Fasel, T. Greber, Surface science at the PEARL beamline of the Swiss Light Source. *J. Synchrotron Radiat.* **24**, 354 (2017).
53. F. J. Garcia de Abajo, M. A. Van Hove, C. S. Fadley, Multiple scattering of electrons in solids and molecules: A cluster-model approach. *Phys. Rev. B* **63**, 075404 (2001).

Acknowledgments: We thank C. Kim, H. W. Lee, K. T. Ko, and M. H. Jo for the fruitful discussions. We also thank H. G. Kim in Pohang Accelerator Laboratory (PAL) for the technical support. We are grateful to the Paul Scherrer Institut, Villigen, Switzerland, for providing synchrotron beamtime at the PEARL beamline of the Swiss Light Source. **Funding:** This work was supported by the Institute for Basic Science (IBS) through the Center for Artificial Low Dimensional Electronic Systems (no. IBS-R014-D1), by POSCO through the Green Science program, by the National Research Foundation of Korea (NRF) through SRC (grant no. 2018R1A5A6075964), and by the Max Planck-POSTECH Center for Complex Phase Materials (grant no. 2016K1A4A4A01922028). S.-Y.C. acknowledges the support of the Global Frontier Hybrid Interface Materials by the NRF (grant no. 2013M3A6B1078872) and POSTECH-Samsung Electronics Industry-Academia Cooperative Research Center. D.Y.K. acknowledges the support by the NSFC of China (grant no. 11774015). K.K. was supported by the NRF (grant nos. 2016R1D1A1B02008461 and 2017M2A2A6A01071297). **Author contributions:** J.S., E.S.A., and J.S.K. conceived the experiments. J.S. synthesized the bulk crystals, and E.S.A. prepared the device of the cleaved crystals. J.S. and E.S.A. performed the transport property measurements. D.Y.K. performed material design based on first principles calculations. K.K., D.W.K., B.G.J., H.K., B.I.M., and J.H.S. performed the electronic structure calculations and the analysis. G.-Y.K., S.-Y.H., and S.-Y.C. carried out structural identification using STEM and the data analysis. G.E. and Jieun Lee performed the MCD experiments and data analysis. S.Y.S. and M.H.J. performed the MOKE experiments and data analysis. Y.J.J. carried out the magnetization measurements. R.S., M.M., Jinwon Lee, and H.W.Y. performed surface characterization using scanning tunneling microscopy and x-ray photoelectron spectroscopy measurements. K.W. and T.T. provided boron nitride crystals. J.S., D.Y.K., E.S.A., S.-Y.C., J.H.S., and J.S.K. cowrote the manuscript. All authors discussed the results and commented on the paper. **Competing interests:** The authors declare that they have no competing interests. **Data and materials availability:** All data needed to evaluate the conclusions in the paper are present in the paper and/or the Supplementary Materials. Additional data related to this paper may be requested from the authors.

Submitted 26 July 2019
Accepted 12 November 2019
Published 17 January 2020
10.1126/sciadv.aay8912

Citation: J. Seo, D. Y. Kim, E. S. An, K. Kim, G.-Y. Kim, S.-Y. Hwang, D. W. Kim, B. G. Jang, H. Kim, G. Eom, S. Y. Seo, R. Stania, M. Muntwiler, J. Lee, K. Watanabe, T. Taniguchi, Y. J. Jo, J. Lee, B. I. Min, M. H. Jo, H. W. Yeom, S.-Y. Choi, J. H. Shim, J. S. Kim, Nearly room temperature ferromagnetism in a magnetic metal-rich van der Waals metal. *Sci. Adv.* **6**, eaay8912 (2020).

Nearly room temperature ferromagnetism in a magnetic metal-rich van der Waals metal

Junho Seo, Duck Young Kim, Eun Su An, Kyoo Kim, Gi-Yeop Kim, Soo-Yoon Hwang, Dong Wook Kim, Bo Gyu Jang, Heejung Kim, Gyeongsik Eom, Seung Young Seo, Roland Stania, Matthias Muntwiler, Jinwon Lee, Kenji Watanabe, Takashi Taniguchi, Youn Jung Jo, Jieun Lee, Byung Il Min, Moon Ho Jo, Han Woong Yeom, Si-Young Choi, Ji Hoon Shim and Jun Sung Kim

Sci Adv **6** (3), eaay8912.
DOI: 10.1126/sciadv.aay8912